ANIMAL ROBOTS

Efficient flapping wing drone arrests high-speed flight using post-stall soaring

Yao-Wei Chin[1,2], Jia Ming Kok[3], Yong-Qiang Zhu[4], Woei-Leong Chan[2], Javaan S. Chahl[5,6], Boo Cheong Khoo[2], Gih-Keong Lau[7]*

The aerobatic maneuvers of swifts could be very useful for micro aerial vehicle missions. Rapid arrests and turns would allow flight in cluttered and unstructured spaces. However, these decelerating aerobatic maneuvers have been difficult to demonstrate in flapping wing craft to date because of limited thrust and control authority. Here, we report a 26-gram X-wing ornithopter of 200-millimeter fuselage length capable of multimodal flight. Using tail elevation and high thrust, the ornithopter was piloted to hover, fly fast forward (dart), turn aerobatically, and dive with smooth transitions. The aerobatic turn was achieved within a 32-millimeter radius by stopping a dart with a maximum deceleration of 31.4 meters per second squared. In this soaring maneuver, braking was possible by rapid body pitch and dynamic stall of wings at relatively high air speed. This ornithopter can recover to glide stability without tumbling after a 90-degree body flip. We showed that the tail presented a strong stabilizing moment under high thrust, whereas the wing membrane flexibility alleviated the destabilizing effect of the forewings. To achieve these demands for high thrust, we developed a low-loss anti-whirl transmission that maximized thrust output by the flapping wings to 40 grams in excess of body weight. By reducing the reactive load and whirl, this indirect drive consumed 40% less maximum electrical power for the same thrust generation than direct drive of a propeller. The triple roles of flapping wings for propulsion, lift, and drag enable the performance of aggressive flight by simple tail control.

INTRODUCTION

The range of flight modes birds can operate in demonstrates that the flapping wing configuration is more versatile than fixed wing and rotary wing designs. Any avian flight starts with takeoff by forceful wingbeats and then settles to an efficient cruise condition before ending with descent and touchdown at low vertical speed using an aerodynamic braking maneuver known as flare (*1*–*4*). Among natural flyers, swifts can fly the fastest in level flight (at 20.8 to 31 m/s) during migration and aerial feeding (*5*). They sometimes fly in an erratic manner at speed chasing each other (*6*–*8*). Aside from accelerating to fly fast, the decelerating maneuver is also helpful for swiftlets to perch and evade obstacles. Swiftlets can pull up a dart (high-speed level flight) to climb before perching (clinging) onto their nest located at the top of a cave (*7*) or a vacant house (*8*, *9*), such as the corner between the ceiling and two walls (see Fig. 1). Before perch, swiftlets need to arrest relatively high-speed flight in addition to staying aloft by hover. These complex acts of aerobatics indoors and outdoors are routinely performed by flying swifts.

Most flapping wing micro air vehicles or ornithopters developed to date can fly forward/backward, circle, and glide, but because of limited excess thrust (*10*–*13*), only a few smaller examples can hover. According to the literature (*14*–*21*), hovering ornithopters have resorted to weight optimization (from a few grams to 20- to 30-g body weight) and enhanced thrust generation by using an X-wing configuration (*17*, *22*–*27*) or multiple wing pairs (*15*, *28*). The first X-winged ornithopter developed by Frank Kieser (*22*, *23*, *29*) could fly forward under the power of a twisted rubber band (*22*, *29*). Later versions of X-winged ornithopters were developed with onboard motor and battery to sustain flight. Examples of hovering X-wing ornithopters include Mentor (*24*), Cornell 3D-Printed Mechanical Insect (*17*), DelFly (*14*, *26*), NUS Flower Fly (*19*), and Robotic Bird (*21*). With enough thrust to hover like helicopters (*30*, *31*), a few tailless ornithopters have managed to perform similar aerobatics, such as hover, a vertical loop by thrust vectoring forward/back and a flip by asymmetric thrust (*16*, *30*, *32*). Recently, insect-inspired drones have adopted multiple wing pairs like X wings (*33*–*35*) instead of a single pair (*36*, *37*) to launch a controlled takeoff and hover using muscle-like electro-active actuators.

Inspired by bats and avian flight, micro air vehicles could adopt similar aerobatic maneuvers to enhance their functionality and to differentiate from other types of small aircraft. A rapid turn using the wings to stop an aerial dart could enable obstacle avoidance in cluttered spaces. A forceful thruster is the prerequisite to aggressive flight with thrust-based tail stabilization and control. Copying the design of a natural flight apparatus is one strategy to improve the flight performance of ornithopters. Examples include (i) light flexible wings capable of passive wing rotation (*36*, *38*, *39*), (ii) wing-wing interaction by clap and fling to enhance thrust generation (*25*, *29*, *40*, *41*), and (iii) elastic storage to recover inertial power (*42*–*49*). However, it emerges that the differences between the drive mechanism (*24*, *50*) and flight muscle have presented a barrier to achieving comparable flight performance. An electric motor can be more powerful than natural flight muscle, as exemplified by the direct drive of spinning propellers in terms of the mass-specific maximum thrust generation (*51*). Indirect drive of flapping wings by motors still underperforms because of inefficient transmission. Recent studies (*47*, *52*, *53*) have shown that frictional power loss in the drive mechanism is more substantial than the aerodynamic and inertial power of flapping wings. There is no clear technological solution to increase performance of miniaturized drives in this application.

[1]School of Mechanical and Aerospace Engineering, Nanyang Technological University, Singapore, Singapore. [2]Department of Mechanical Engineering, National University of Singapore, Singapore 117575, Singapore. [3]Aerospace Division, Defence Science and Technology Group, Edinburgh, SA SA5111, Australia. [4]School of Mechanical and Automotive Engineering, Qingdao University of Technology, Shandong, China. [5]School of Engineering, University of South Australia, Mawson Lakes, SA 5095, Australia. [6]Joint and Operations Analysis Division, Defence Science and Technology Group, Edinburgh, SA, Australia. [7]Department of Mechanical Engineering, National Chiao Tung University, Hsinchu 30010, Taiwan.
*Corresponding author. Email: mgklau@nctu.edu.tw

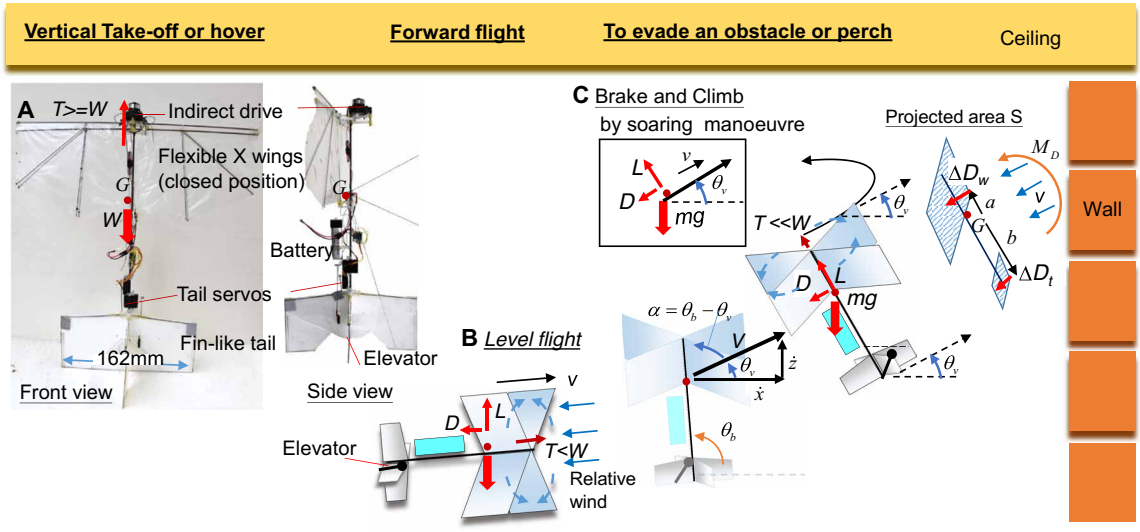

Fig. 1. Aggressive flight maneuvers by X-winged ornithopter with tail control. (**A**) Hover (at upright body attitude $\theta_b = 90°$) with thrust T being equal or greater than weight $W = mg$. (**B**) Level flight (nearly level $\theta_b \approx 0°$) at relative high speed v that induces lift L against weight. (**C**) Brake and climb by tail elevation and wing dynamic stall using the soaring maneuver. Then, the ornithopter translates at velocity v at an angle θ_v, and it is thus subjected to lift L and drag D at the angle of attack $\alpha = \theta_b - \theta_v$. As shown in the inset of the free-body force diagram, the weight W and drag D help rapid flight arrest. This soaring maneuver leads to a climb while braking. Meanwhile, the asymmetric drag distribution between wings and elevated tail induced a turning moment $M_D = \Delta D_w a - \Delta D_t b$, where ΔD_w and ΔD_t are drags that act momentarily on the wing and tail, respectively, at distance a and b off the center of gravity G, respectively.

Although aerodynamic performance of flapping wings has been reported to be comparable to spinning propellers (*24*, *54*), if not better (*55*–*57*), previous indirect drive of flapping wings did not perform better than direct drive of propellers in terms of electrical power loading, i.e., thrust per unit electric power (*49*). Similarly, geared drive of a larger propeller was reported to suffer from additional frictional power loss in the gearbox; it thus became less efficient as compared to direct drive of a smaller propeller (*58*–*60*) despite being advantaged with lower disk loading (T/A) (*4*, *24*, *61*). We hereby compare indirect drive of flapping wings with direct drive of a spinning propeller to unravel the complex interplays among drive, transmission, and aerodynamics.

Here, we identified shaft whirl (or wobble) shown in Fig. 2 to be the cause of most mechanical loss in reciprocating the set of flapping wings. Furthermore, we found the problem of shaft whirl (*62*–*64*) to be an issue for the direct drive of a spinning propeller, causing substantial frictional power loss. To maximize thrust output by flapping wings, we designed and developed a low-loss transmission that used an anti-whirl elastic mechanism and bearings. This efficient transmission yields forceful flapping wing propulsion to perform energetically costly aerial tasks such as hover, acceleration, and an aerial dart. Furthermore, using our design, we show that a soaring maneuver supports a vertical climb and an aerobatic turn by arresting the fast aerial dart, without the need to increase throttle (Movie 1). A prerequisite to this maneuver is the initial condition of high-speed dart and subsequent dynamic stalling (*4*, *65*) of wings in a rapid pitch up by tail elevation like birds do (*66*, *67*). Likewise, the same soaring effect was exploited to help pull up and arrest the ornithopter from a nose-down dive.

RESULTS

Ornithopter design and principle of operation

Figure 1A and fig. S1 show our 26-g prototype tailed ornithopter with four flexible wings of 280-mm span. A low-loss transmission with anti-whirl features and elastic storage provided the indirect drive of these flapping X wings. The anti-whirl features included tandem nylon hinges and double shaft bearings to suppress the flapping-induced rocking that tends to disengage or bind the transmission and gear train. In addition, tandem nylon hinges provided partial elastic storage to recover the wing kinetic energy during their deceleration at extrema. Under full throttle drive by a small motor (HobbyKing AP03 7000 kV, 3.1 g) at its rated 4.2 V, this optimized drive of 14- to 15-Hz flapping X wings produced nearly 40 g of static thrust, as much as the static thrust generated by the recommended 82.25-mm diameter propeller (Prop 3020). In turn, the excess thrust can power the energy-costly hover and accelerate a fast dart while producing strong downwash around the tail to stabilize flight.

This tailed ornithopter with flexible X wings is passively stable in both hover (vertically) and glide (at level body pitch attitude) when the tail elevator was set to the neutral position. Similar to birds (*66*, *67*), this ornithopter could also be trimmed (i.e., adjusted) by tail elevation under pilot control to fly at different attitude. Hover stability at vertical body attitude with neutral elevator was achieved by the pendulum effect (*15*, *68*, *69*) with the placement of thrust-generating wings above the center of gravity. However, when the body was turned 90°, its forward glide stability could not be assured by the lift-generating wings, which were ahead of the center of gravity, similarly to the forward placement of canard wings (*30*, *31*). To achieve glide stability, we purposely have (i) axial symmetry of X wings and "+" shape fin-like tails, (ii) the center of gravity placed closer aft of the aerodynamic center, (iii) a relatively large horizontal tail plane area being 35% of the wing plane area, and (iv) a small longitudinal dihedral (<5°) at neutral elevator position. High-authority flight control and stability are possible when provided with high thrust that induces strong downwash around the tail. Tail elevation can control the mode of flight, for example, neutral elevator for vertical climb and side elevator for turning sideways. In this way, there is no need to

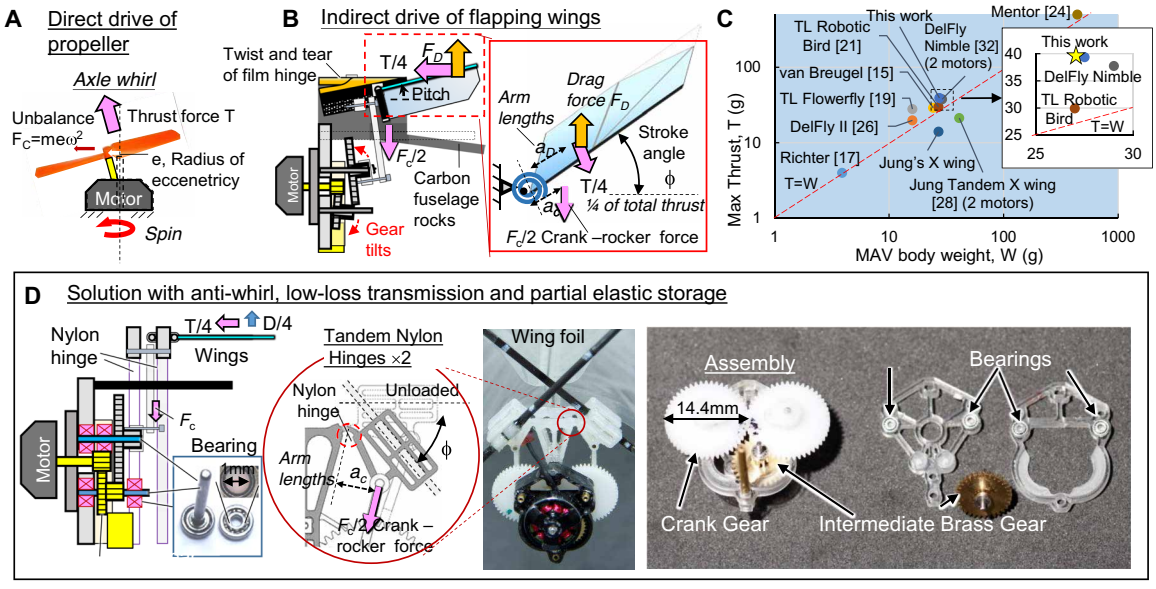

Fig. 2. Effect of axle whirl on the drive of propulsion. (**A**) Direct drive of a spinning propeller (subjected to centrifugal force $F_c = me\omega^2$). (**B**) Indirect drive of flapping wings (subjected to crank-rocking force $F_c/2$ at an arm length a_c). During wingbeat at stroke angle ϕ and wing rotation β, the drive of each wing needs to overcome drag force F_D to produce thrust $T/4$. (**C**) Reported thrust generations by flapping X wings relative to the body weights of micro air vehicles. (**D**) Our proposed transmission design to suppress the axle whirl by using tandem pairs of bearing and nylon hinges.

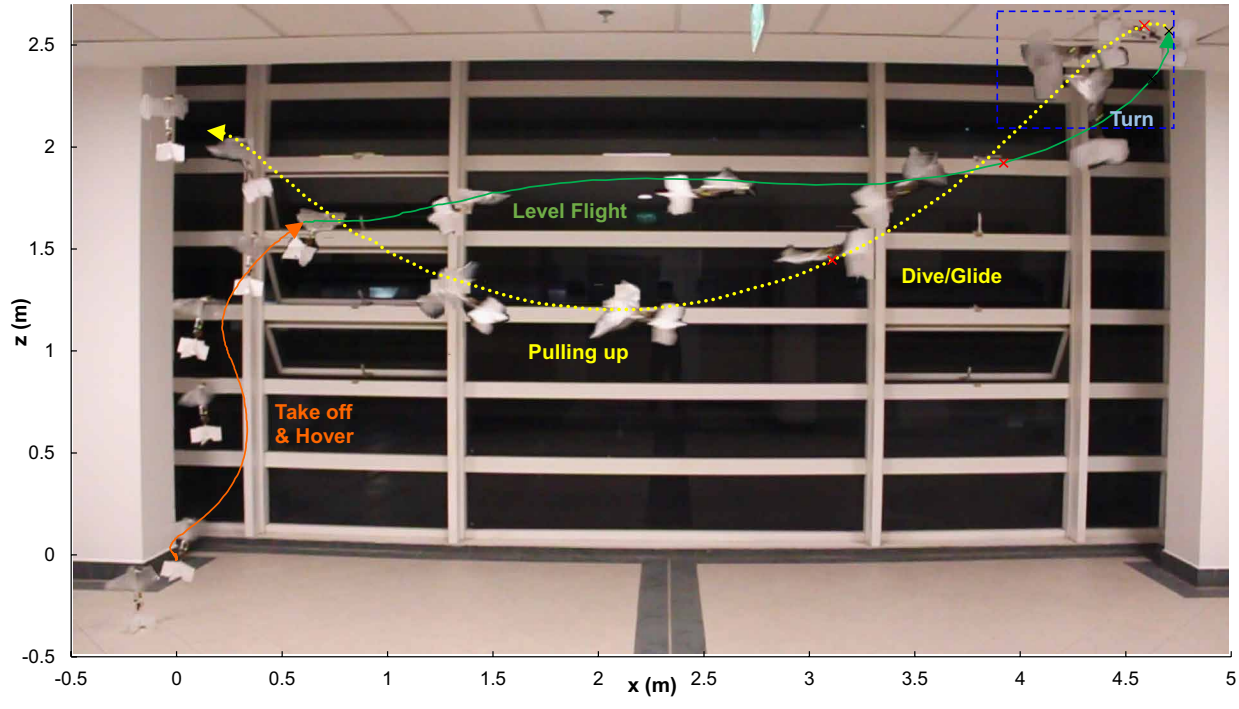

Movie 1. Multimodal flight including aerobatic turn by X-winged ornithopter.

shift the center of gravity, as in previous work (*69*), when the ornithopter needs to switch the flight mode from hover to forward flight.

Here, we demonstrated the soaring maneuver of an ornithopter to climb by air brake. Our analysis focuses on (i) the dynamics of flying a rapid turn with the help of drag on flapping wings and (ii) frictional power loss in the drive mechanism for a flapping wing thruster.

Aerobatic maneuvers

We showed that an aerobatic turn (greater than 90° flip) is the result of dynamic stall of the wings and tail elevation during the "soaring" maneuver that arrests a fast dart. The soaring maneuver describes the climb by air brake similarly to that performed by soaring birds in the presence of wind. Likewise, the same maneuver also happens

when pulling up a dive, albeit the direction is rotated by 90°. As shown in the free-body force diagram of Fig. 1C, weight *mg* and drag *D* assist in rapid deceleration (stopping a dart) when soaring up to 90° pitch

$$m\frac{dv}{dt} = -mg\sin\theta_v - D \quad (1)$$

where v is the dart speed along the flight path and θ_v is the velocity angle. The parachuting effect of drag also helps gliding animals, such as flying squirrels, to soar to a 90° angle of attack before landing on a tree trunk at the end of a glide (*1*). This strategy can be equally useful for an ornithopter to land upside down on a surface (a bat-like flip) or to arrest rapidly while stopping a dart.

Like birds (*66*, *67*), tail deflection by this ornithopter creates substantial pitching moment provided in either high-speed free stream– or strong thrust–induced downwash. In the case of a fast dart, forward air speed dominates thruster's downwash. Hence, the tail moments induced by the former can initiate the pitch up of the ornithopter, increasing the angle of attack of the flapping wings. The post-stall of wings and tails can quickly decelerate the ornithopter. The drag coefficient for the wing and tail can be estimated from $C_D = 2\Delta D/(\rho v^2 S)$, where S is the total projected area of the wing or tail normal to the flight path. The ratio of the projected area to the plane area is $S/A_0 = \sin(\theta_b - \theta_v)$ (see Fig. 1C). Experiments show that the drag coefficient can be as high as 2.8 during air brake. Calculation of nondimensional aerodynamic coefficients is elaborated in Supplementary Text.

As the soaring (translation) path goes to a vertical climb ($\theta_v = 90°$), the ornithopter body turns simultaneously ($\theta_b > 90°$) with the help of drag-induced pitching moment. Because of the plane area difference and tail elevation, the drag acting on the wings is greater than that on the tail. The asymmetrical drag distribution creates a substantial pitching moment M_D to flip the ornithopter following

$$J_G\ddot{\theta}_b = \Delta D\left[\left(\frac{S_w}{S}\right)a - \left(1 - \frac{S_w}{S}\right)b\right] \quad (2)$$

where J_G is the mass moment of inertia of the whole ornithopter about the center of gravity *CG*, ΔD is the sum of wing and tail drags, S_w is the projected area of X wing in the normal, and a and b are the distance of the drag force center to *CG* for the wing and tail, respectively. The pitching moment increases with increasing dart speed. While the dart speed starts to decrease beyond the stall angle, the drag generating area increases until the wing plane becomes normal to the dart direction. In this way, the ornithopter can flip rapidly beyond 90° pitch. This analysis suggests that the routine execution of flips by swifts and bats during perching could be achieved by arresting a dart.

Figure S9 shows the feasibility of other drones performing a flight arrest. In principle, both ornithopter and fixed wing aircraft can maneuver a post-stall arrest of flight by a rapid pitch up. However, this soaring maneuver requires enough initial kinetic energy to convert into gravitational potential energy. To date, a few fixed wing aircraft have demonstrated level perching (*70*) but not climbing by post-stall arrest. High thrust is needed to prevent a fall during the flight arrest. In comparison, a quadcopter has neither lift-generation or drag-generation surfaces to command airbrake. To arrest forward flight, the quadcopter body needs to revert backward with thrust opposing the forward motion. In some special cases, contact by corner impact helped arrest the quadcopter flight in preparation for perching to a vertical wall (*71*).

Power requirement and friction in the thruster

Flight muscles drive flapping wings of natural flyers (*1*, *2*); a brushless motor is the choice of drive for powered micro air vehicles, either direct drive of a propeller or indirect drive of flapping wings (see Fig. 2). A typical indirect drive for flapping wing ornithopters consists of a gear train and a crank-rocker mechanism (*24*, *50*, *72*). The transmission leverages the output torque required for forceful wingbeat by reducing a high motor spin rate f_m to a low wingbeat frequency f. Meanwhile, the double crank-rocker mechanism is responsible for converting rotary spin of the drive motor into a sweeping wing stroke 2Φ. However, the transmission is far from perfect as was assumed in previous studies (*24*, *47*). In particular for a small-motorized drive, the frictional power loss is higher than aerodynamic and inertial power alone (*47*, *49*).

Transmission whirl may happen and cause substantial frictional power loss in fast spinning propellers under direct motorized drive (*62*–*64*). It was thought to be a minor effect in wing-reciprocating transmissions that drive at reduced speed. However, the high reciprocating force required for wingbeat will rock a poorly supported spinning shaft in a gear train, whirling and thus compromising efficiency. For example, in our previous design of indirect drives (*49*), the rotating gears in the transmission were observed to whirl about a cantilevered pin, causing wear in the bore (see Fig. 2B). An efficient transmission requires bearing support (see Fig. 2D) to suppress shaft whirl despite the stringent weight constraints.

In short, for a motorized flapping wing drive, mechanical shaft power output is expended to work against loads and friction

$$P_{\text{mech}} = P_{\text{load}} + P_\mu \quad (3)$$

This load power P_{load} is required to work against the total torque, Q_{load}, which is the sum of the aerodynamic drag torque, inertia, and elastic torque of the four flapping wings on elastic hinges

$$P_{\text{load}} = Q_{\text{load}}\dot{\phi} = (4F_D\bar{a}_D + 4J_w\ddot{\phi} + 4k\phi)\dot{\phi} \quad (4)$$

where F_D is the drag force acting on each flapping wing (thruster) at the force center away from the wing pivot by an equivalent arm distance $\bar{a}_D$, J_w is the rotational inertia of each wing, and k is the torsional spring constant of each elastic hinge. In the case of harmonic wingbeat $\phi = \Phi\sin 2\pi ft$, the stroke speed amplitude is $2\pi f\Phi$, with f being the wingbeat frequency and Φ being the angular stroke amplitude.

When a double crank-rocker mechanism is used to drive two pairs of flapping X wings, a crank-rocker force F_c acts on the wing base of each wing pair at a distance a_c away from the fulcrum (pivot). This, in turn, produces the total load torque $Q_{\text{load}} = 2F_ca_c$ for driving the two wing pairs. This normal force tends to tilt the shaft off the axis of the bearing bore, causing extra rubbing between the whirling shaft and the bearing bore. In turn, this leads to substantial frictional power loss and bore wear. The frictional power loss can be calculated as the product of induced frictional force and the rubbing speed at the interface of frictional coefficient μ following

$$P_\mu = 2\mu F_c r_b(2\pi f n_c) = \mu\left(\frac{bn_c}{a\Phi}\right)P_{\text{load}} \quad (5)$$

where r_b is the radius of bearing bore in contact with the spinning shaft and n_c is the speed reduction ratio by crank-rocker mechanism (*49*). This shows the frictional power loss being linearly proportional to load power. This explains why higher thrust is associated with

more frictional power loss being incurred. The obvious solution to reduce the friction is by using a shaft bearing.

A small brushless motor of limited torque output cannot directly drive the high load of flapping wings and associated friction. A speed reduction gear train was used to reduce the reactive load and thus improve the motor efficiency, which follows (*59*, *60*)

$$\eta = \frac{P_{\text{mech}}}{IV} = \frac{K_t I 2\pi \text{nf}}{IV} \tag{6}$$

where $f_m = nf$ is the motor rate of rotation and n is the total speed reduction ratio, which reduces the reactive load torque Q_{load}/n. This formula suggests that motor efficiency increases in proportion to the motor rotation speed. Ideally, the drive efficiency is maximized at full throttle; this is desirable during the energetically costly flight operation, such as hover and ascent.

Re-expression of the equation above further shows linear proportionality between the load torque and electrical power input

$$Q_{\text{load}} \propto \frac{P_{\text{mech}}}{2\pi nf\Phi} = \left(\frac{K_t}{\Phi V}\right) IV \tag{7}$$

from which we can deduce that aerodynamic force, either thrust or drag, of flapping wings will be linearly proportional to the electrical power input IV. Departure from ideal linearity may happen when drive performance deteriorates. For example, prolonged drive and temperature elevation might cause reduction in battery output voltage (*24*). Furthermore, the input electrical power to the motor depends on the conversion efficiency of the electronic speed controller, which decreased substantially with respect to increasing load according to (*59*).

The same power analysis can also be applied to the direct drive of a two-blade propeller. On the assumption that the same drag was required for the same thrust generation, the load torque increases with increasing radius of the propeller. Load torque further increases because of the friction between high-speed turning shaft and bearing. Hence, the total mechanical power incurred is the sum of load- and friction-induced power when the propeller spins at angular speed ω following

$$P_{\text{mech,prop}} = 2 F_d \bar{r}_d \omega + \mu_B F_C(\omega)\, r_B \omega \tag{8}$$

where the first term is the aerodynamic power induced by mean drag force F_d acting on each blade of the propeller at radial position $\bar{r}_d$ off rotation axis, spinning at an angular speed $\omega = 2\pi f_m$. The second term is the frictional power loss induced by the centrifugal force of the propeller/shaft, which acts normal to the bearing bore of radius r_B with frictional coefficient μ_B. The centrifugal force $F_C(\omega) = me\omega^2$ was caused by the rotating unbalanced mass m of the whirling propeller at radius of eccentricity e off the axis of rotation. Although the frictional coefficient of bearings is low, the high propeller rotational speed combined with high normal force can lead to non-negligible frictional power loss. This formula suggests that a smaller propeller requires less torque to drive as compared to a larger propeller, if the frictional power loss was comparable.

Wing kinematics, thrust, and power expenditure

We conducted a static thrust test of flapping wings, under indirect drive by a small brushless motor (AP-03 7000 kV, 3.1 g). Figure 3 and movies S1 and S2 show the wing kinematics, whereas Fig. 4 shows the mean thrust generation with respect to drive parameters. Figure 3B shows that the wing stroke angle 2Φ is nearly constant at the designed 50°, largely independent of the wingbeat frequency. Meanwhile, the wing pitch amplitude B increases with increasing wingbeat frequency, i.e., $B \propto f$, because of increasing inertial and aerodynamic loads (*73*), but the maximum wing pitch amplitude tapers toward full throttle drive because of wing membrane tension (see fig. S2). Also shown in Fig. 3 (B to G) are the frequency dependence of wing stroke, pitch, and their rates and the time profiles over a cycle of wingbeat.

Next, we studied the effect of elastic hinges on wing kinematics given the same drive and transmission. The benchmarks are conventional pin-jointed X wings, which show little elastic resistance to wing opening as compared to the nylon hinges (see fig. S2). The wing kinematics does not change much with the kind of wing-base joints, except the induced pitch speed. Figure 3C shows that the peak pitch speed amplitude with nylon-hinged wings rose to 60 rad/s under full throttle drive, whereas that of the pin-hinged X wings tapered to 50 rad/s under the same drive. The elastic recoil enables more forceful wingbeat by faster wing pitch speed. As a result, the drive of nylon-hinged wings requires 13% less electrical power than the drive of pin-joined ones for the same thrust generation near full throttle (see Fig. 4, D and E). The maximum electrical power loading of the former drive is 6.4 g/W at full throttle, whereas that of the latter drive is lower. Maximum electrical power loading at full throttle drive is good for energetically costly hover and ascent flight.

It is commonly thought (*13*, *57*) that direct drive of a spinning propeller is more efficient than indirect drive of flapping wings for micro air vehicles. To show that this is not the case, we compared these two distinct drives with the same motor. Figure 4 (A and B) and table S1 show five propeller designs obtained from the market. The propeller radius (weight) ranges from 80.2 mm (1.37 g) for Prop 3020 to 177.05 mm (2.89 g) for Prop 7035. Figure S7 shows the test setup for propeller static thrust measurement. The smallest propeller (Prop 3020) performed the best. Its full-throttle electrical power loading is 4.6 g/W, lower than the maximum of 4.8 g/W near half throttle. The electromechanical conversion rate at full-throttle direct drive was 49% when the propeller spun at 233 Hz (see Fig. 4D). Its electrical losses included resistive and windage losses and the loss in the electronic speed controller (*59*, *60*), whereas the mechanical losses include substantial frictional power loss caused by axle whirl. Hence, Fig. 4C shows electrical power loading (*T/IV*) being lower than the mechanical power loading (i.e., the ratio of thrust to mechanical power, $T/K_t I\omega$), which is proportional to aerodynamic efficiency (*24*).

Axle whirl is a classical problem for cantilevered propeller and rotor machinery (*62*, *63*). It is less a problem to a larger propeller that spins at a slower speed with proper balancing because of gyroscopic effect as described by the classic textbook (*64*). However, we found that axle whirl is substantial with the small propeller tested (Prop 3020 of 82.25-mm diameter and 1.37 g) that spun at 233 Hz. Figure 5 shows the total force vector generated by three different propulsive devices—namely, a small propeller (Prop 3020), a larger propeller (Prop 6030), and large flapping X wings of 280-mm span—generating nearly the same mean thrust (see Fig. 5E). Axle whirl induced radial forces in addition to vertical thrust. The Lissajous curve of the radial force induced was found to be skewed rather than circular because of the complex interaction between bearing, spinning propeller, and axle (*62*). Then, full-throttle drive of Prop 3020 had an amplitude of radial force 3.9 times that of vertical thrust. Figure 5 (C and D) shows that there is a large-amplitude variation in the vertical thrust

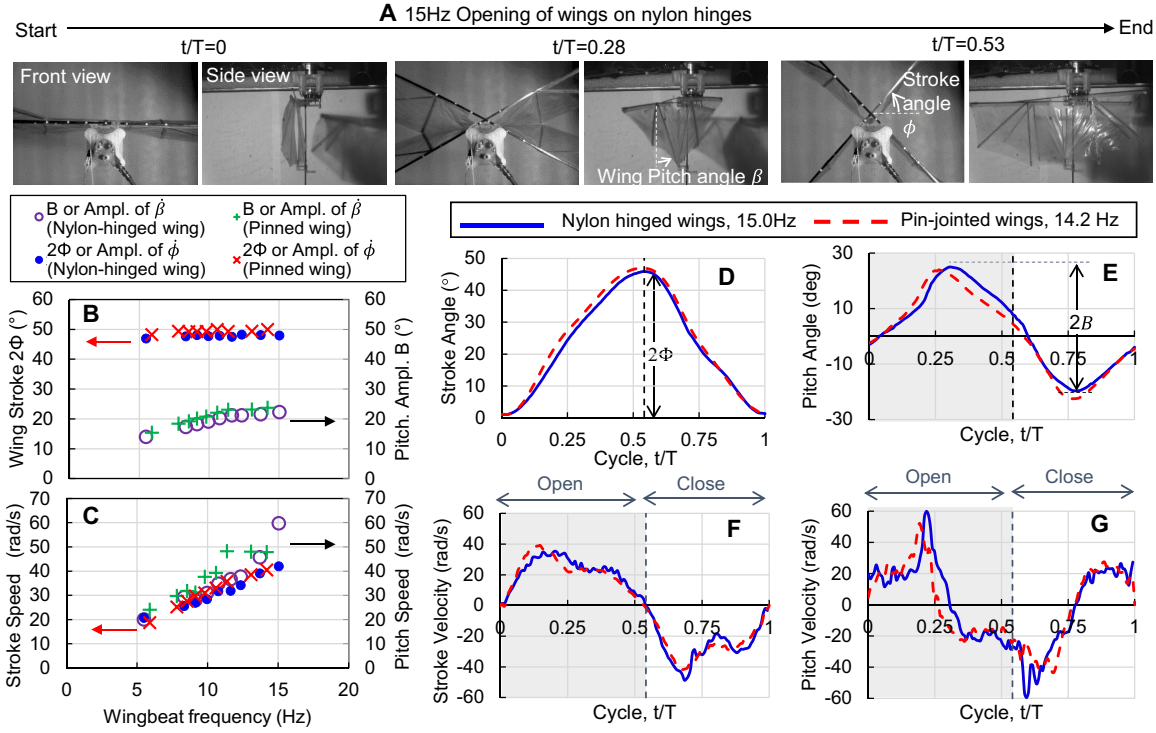

Fig. 3. Wing kinematics of flapping X wings under indirect drive via anti-whirl mechanism. (**A**) Snapshots of the nylon hinged X wings moving from closed to open at 15 Hz (maximum throttle) (see movies S1 and S2 for top and side views, respectively). (**B** and **C**) Frequency dependence of wing stroke 2Φ and pitch amplitude *B*, the rates of wing stroke angle and pitch angle, respectively ($\dot{\phi}$ and $\dot{\beta}$), (**D** to **G**) and their time profiles for 1 cycle of wingbeat at 14 to 15 Hz.

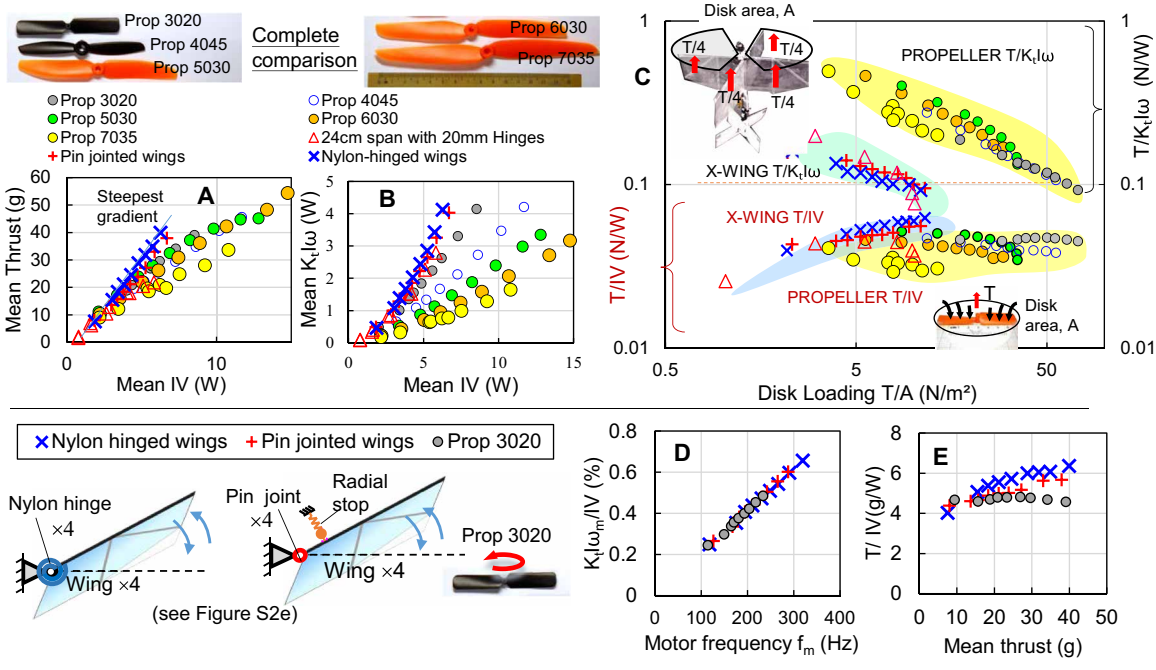

Fig. 4. Performance comparison between flapping wing and rotary propulsions. (**A**) Comparison by thrust generated (*T*) as a function of input electrical power (*IV*). (**B**) Comparison by output shaft power (K_t I ω) as a function of input electrical power (*IV*). (**C**) Comparison by effect of disk loading (*T*/*A*) on either electrical power loading (*T*/*IV*) or mechanical power loading [T/(K_t I ω)]. (**D** and **E**) Comparison by effect of elastic storage on indirect drive of flapping wings in terms of motor conversion efficiency (K_t I ω/IV) and electrical power loading.

component despite nearly constant power expenditure. The indirect drive of flapping X wings also shows radial forces due to the out-of-phase interaction between rocking fuselage and flapping wings, whereas the drag and inertial forces in the symmetrically configured flapping X wings should cancel out each other. Estimates of axle eccentricity from the radial force amplitudes (see table S2) showed that the indirect drive of flapping wings was subject to the least whirl although the drive motor spun faster than direct drive of the propeller.

Our experimental results showed that drive efficiency for flapping propulsion was higher than that for rotor propulsion with the small motor tested. By exploiting the lower disk loading of large wing sweep area (see Fig. 4C and table S2), flapping X wings can beat 21.3 times slower than a propeller spins to produce the same amount of thrust (see Fig. 5E). Furthermore, according to Eq. 7, the gear train helps to greatly reduce reactive load such that the drive motor can spin faster (see Fig. 4D). This leads to higher motor efficiency for full-throttle indirect drive of flapping X wings, for example, up to 66% (at 319-Hz spin) for driving nylon-hinged wings and up to 60% for driving pin-hinged wings. According to Eq. 8 and Fig. 4C, a higher reactive load of a larger propeller also explains its poorer drive efficiency despite its better aerodynamic efficiency as compared to smaller propeller.

Aerobatic flight

With nearly 40% excess maximum thrust (see Fig. 2C and table S3), this ornithopter can hover and ascend (see movie S3). Figure 6 and movie S4 show a complete execution of various flight modes with smooth transitions. These flight modes started from a vertical takeoff and climb, hover, transit to a level forward dart, air brake, and soar to a height before reversing the flight path, diving, and finally landing with upright body attitude. A transition from hover to forward flight risked a dip due to reduced vertical component of thrust, but once it flew forward, extra lift was gained because of increasing free stream speed (see figs. S3 and S4 and movie S6).

Next, we considered the flight conditions to execute an aerobatic turn. Before post-stall arrest, Fig. 6 (A and B) shows that the ornithopter darted for 3 to 4 m and reached a maximum speed of 6.1 m/s at $\theta_b = 40°$ to 45°. Subsequently, the post-stall arrest achieved a maximum deceleration of 31.4 m/s^2, followed by a tight corner flip of 31.6-mm radius from upward body attitude to backward level. This maneuver requires tail elevation to initiate a rapid body pitch and to dynamically stall the wings at high dart speed. Like the soaring maneuver, the process was accompanied by a height gain at the expense of speed loss because of conversion of kinetic energy to gravitational potential energy, following the displacement integral of Eq. 1. While the ornithopter was rising to the peak of height, the throttle was reduced as indicated by a dip in wingbeat sound intensity amplitude (see Fig. 6C). Following a back turn, a pull up from the dive was demonstrated by throttling up the flapping wings and elevating the tail.

The dart speed determines how fast the subsequent soar and how sharp the subsequent flip can be. However, it is the glide stability that matters to the recovery from 90° flip without tumbling at a slow speed. To prove this, we piloted another aerobatic flip immediately followed by an unpowered glide. Before the flip, the demonstrated dart speed was 4.2 m/s after a 1.5-m dart. Figure 7 and movie S5 show that this ornithopter quickly recovered its glide stability, descending stably at level body attitude ($\theta_b = -180°$) without tumbling right after the execution of a 90° flip in a 75.0-mm radius. To execute a successful flip, the response time of pilot and space must be suitable. Movie S6 and fig. S4 show that the ornithopter continued a high-speed dart of 8 m/s when not pitched up in time given the limited flight arena.

Next, we tested whether this ornithopter can slow down and deflect a nose-down dive by a stick-free tail pre-elevation (see Figure 8). In the tests [see Fig. 8 (A and B) and movies S7 and S8], the ornithopter was released from a height nose down; the flight path and body pitch attitude were recorded (see fig. S5). Movie S7 shows the nose-down dive of the ornithopter with neutral tail elevation ($\delta_e = 0°$). Its sink was fast (taking less than 0.5 s to lose 2.3 m of altitude), but it did not manage to nose up given its small inherent longitudinal dihedral at the neutral tail position. Movie S8 shows that full tail elevation ($\delta_e = 40°$) helped quickly turn the body attitude once the ornithopter gained enough speed. The maximum sink speed was 11 m/s (after 1-m sink). Subsequently, the nose-up glide (up to $\theta_b = 55°$) continued at nearly constant sinking rate of half the maximum value. In a separate dive from an 8.3-m height (see Fig. 8E and movie S9), the ornithopter was pulled up from an unpowered nose dive. At the end of the dive, the X wings were throttled up to recover from the dive to avoid a hard landing.

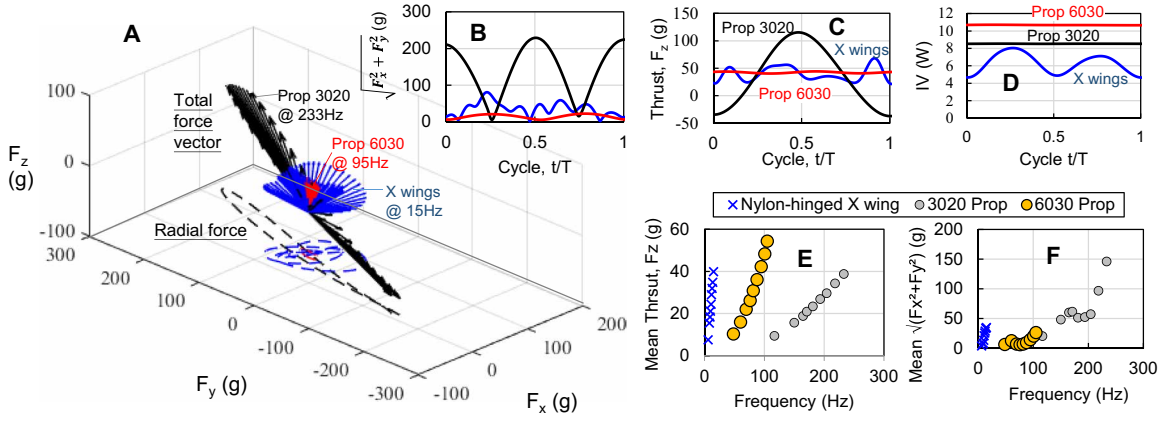

Fig. 5. Axle whirl observed in the drive of flapping X wings and spinning propellers. (**A**) Vector plot of total force generation over a cycle together with Lissajous curve of radial force projected on the *x*-*y* plane. (**B** to **D**) Time profiles of radial force generation, thrust generation, and electric power expenditure during a cycle of spin or flap. (**E** and **F**) Frequency dependency of vertical force component (thrust) and radial force component of propulsion.

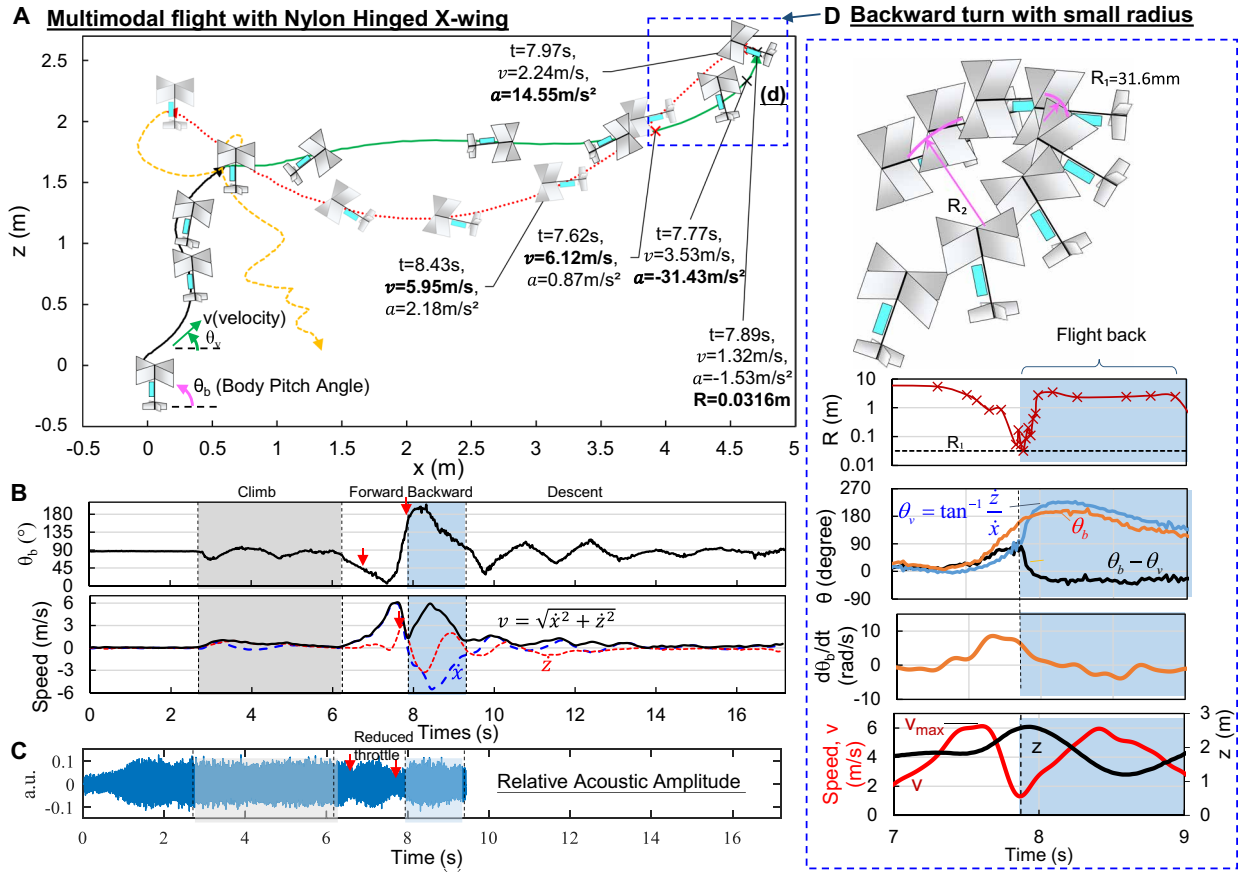

Fig. 6. Aerobatics performed by the nylon-hinged X-winged ornithopter. See movie S4. (**A**) Trajectories (in *x* and *z* coordinates) of multimodal flight, which includes hover (black line), transition to fast forward flight (green line), short turn (blue box), backward dive (red line), and descent and landing (yellow line), with velocity (*v*) and acceleration (*a*) indicated at particular times (*t*). (**B**) Time profiles of body pitch angle (θ_b) and speed ($v = \sqrt{\dot{x}^2 + \dot{z}^2}$) during the multimodal flight. (**C**) Time profile of wing-beat sound intensity (in relative arbitrary unit) during the multimodal flight. (**D**) Zoomed-in view of the backward turn performed and the time profiles of the turn radius (*R*), attitudes of velocity and body (θ_v, θ_b), rate of body attitude change $d\theta_b/dt$, and speed *v*.

These observations of changing body pitch attitude during the unpowered dive provide a simple basis for analyzing stick-free glide stability. According to stability theory (*30*, *31*, *66*, *67*, *74*), an aircraft is passively stable when the total induced moment *M* about its center of gravity tends to counter the angular perturbation $\Delta\theta_b$ following

$$\frac{\Delta M}{\Delta \theta_b} = \text{negative} \quad (9)$$

During the dive, the ornithopter of body pitch attitude (θ_b) was subject to pitching moment as induced by the free stream, which varies in speed *v* and direction (θ_v). The induced moment can be estimated as $M = J_G\ddot{\theta}_b$, where J_G is the ornithopter's moment of inertia about its center of gravity and $\ddot{\theta}_b$ is the angular acceleration calculated as the second-order time derivative of the measured body pitch attitude. To rule out the effects of varying flight parameters, we plotted the coefficient of moment $C_M = 2M/(\rho V^2 Ac)$ instead of the moment with respect to the angle of attack ($\alpha = \theta_b - \theta_v$), where *A* is the total plane area and *c* is the wing chord width. The plot (Fig. 8D) shows that the ornithopter with full tail elevation is passively stable in glide but, with neutral tail positioned, becomes neutrally stable.

DISCUSSION

The dual stability to hover and glide is desired for an ornithopter, enabling manual flight control by the pilot. However, the means of hover stability differs from that of glide stability. The flexible flapping wings behave differently from canard fixed wings and thus end with a different stability outcome, although they are placed ahead of the center of gravity (*30*, *31*, *74*). Furthermore, the drag on the flapping wings of birds and ornithopters cannot be neglected (*66*, *67*), unlike the assumption of negligible drag on fixed wings for conventional analysis. Here, we proposed the thrust-based stabilization by fin-like tail to explain the hover stability; second, we explain the neutral glide stability at neutral tail elevation by the fact that the tail leads the flexible wings to respond to rigid-body perturbation.

Let us first analyze the static hover stability (see Fig. 7B). During the normal hover in still air, four X wings beat to counter gravity ($m = 26g$), moving the air downward. As a reaction to the 26*g* thrust force, the downwash gains speed *w* of 1.23 m/s according to disk actuator theory (i): $w = \sqrt{mg/(2\rho R^2\phi)}$, where the corresponding disk has a total swept angle $\phi = 200°$, radius $R = 0.14$ m, and air density $\rho = 1.225$ kg/m^3. When the ornithopter body was perturbed by a small angle $\Delta\theta_b$, the downwash momentarily stays its course because of fluid inertia. Then, the rigid tail follows the rigid-body

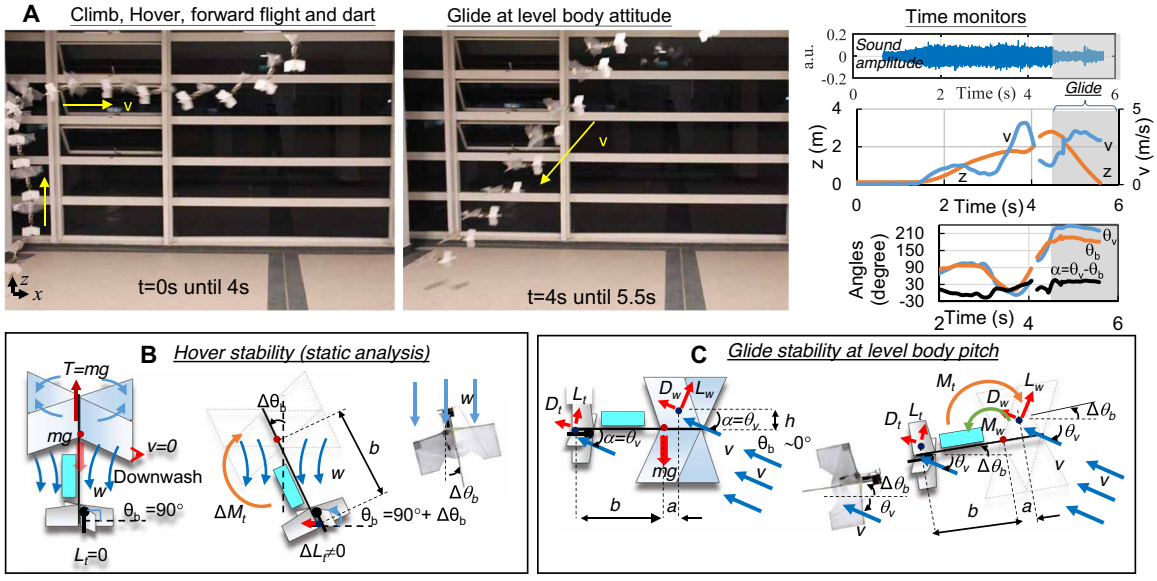

Fig. 7. Flight stability analysis. (**A**) Recovery of flight stability right after a flip (see movie S5) and time monitors of wingbeat sound amplitude, height (z), speed (v), angles of velocity θ_v and body pitch θ_b, and angle of attack $\alpha = \theta_v - \theta_b$. (**B**) Free-body force diagram for hover stability analysis shows as the reaction of thrust generation T at still air $v = 0$, downwash of nonzero speed w induces tail lift ΔL_t and, thus, tail moment ΔM_t (about the center of body mass at a distance b) that stabilizes the hovering against body perturbation $\Delta\theta_b$. (**C**) Free-body force diagram for glide stability analysis shows that free stream of constant speed v induces lifts and drags L_w, L_t, D_w, and D_t at the wings and tail, respectively. These aerodynamic forces on wings and tails, in turn, induce the wing moments M_w and tail moments M_t about the center of body mass. Then, the ornithopters were trimmed to glide at neutral stability against perturbation with the help by wing flexibility.

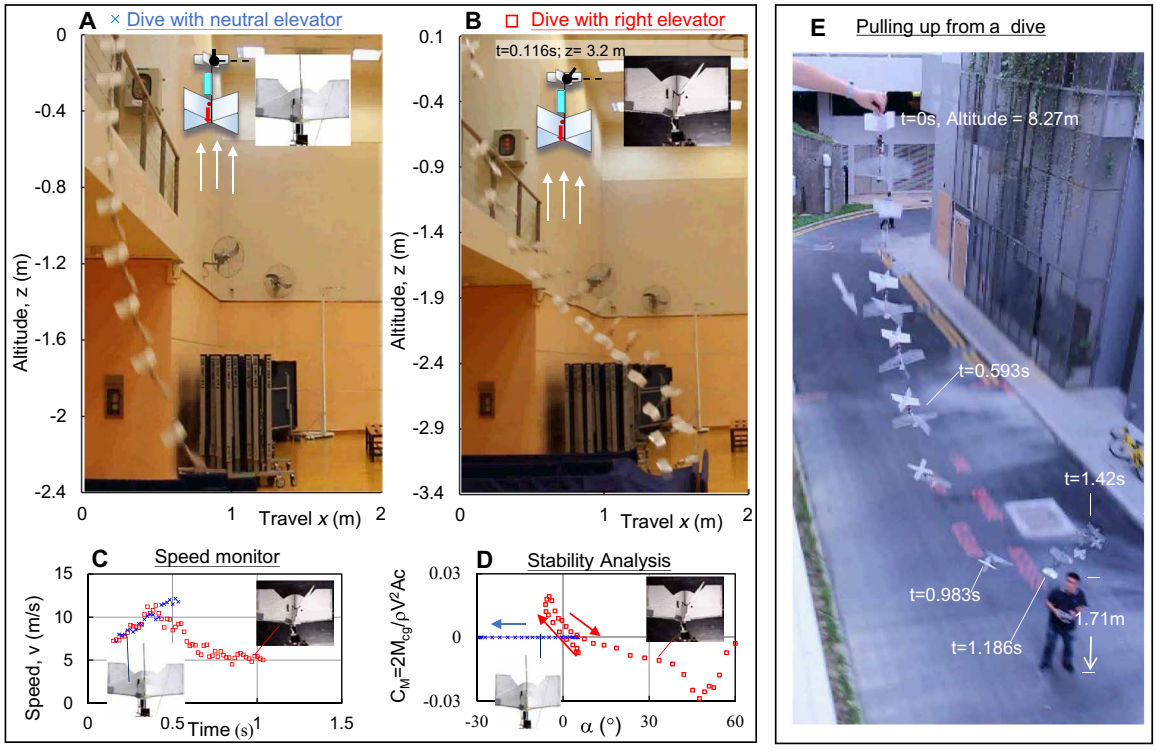

Fig. 8. Ornithopter capable of pulling up from a nose-down dive. (**A** and **B**) The effect of elevator position on the flight path of unpowered nose-down dive (see movie S7) with tail neutral and (movie S8) with tail pre-elevated. The stability analysis by (**C**) monitor of speed and (**D**) plot of moment coefficient with respect to the angle of attack. It was shown that the pre-elevated tail helped stabilize the flight further. Subsequent demonstration in (**E**) further showed a successful pull up from a dive, which was followed by a powered climb to hover (see movie S9).

motion with the angle of attack becoming $\Delta\alpha_T = \Delta\theta_b$ with respect to the downwash. This induces a tail lift ΔL_t and a stabilizing moment following

$$\Delta M_T = -\Delta L_T b \tag{10}$$

where b is the distance between the tail's aerodynamic force center and the ornithopter's center of gravity. Flexible wings are subject to a slower stream during normal hover and thus do not contribute much to destabilizing moment. This thrust-induced stabilization by tail is high during climb and hover but becomes less during descent. This explains the observation (in Fig. 6A) that the ornithopter body swung more severely during descent than it did during ascent.

Next, we analyzed the glide stability (see Fig. 7C). As shown in the free-body force diagram, this ornithopter was trimmed to glide with level body pitch attitude, at angle of attack α relative to the wind. Both the wings and tail generate aerodynamic forces (lift and drag) to support the body weight and counter the tendency to rotate. Then, the wings are subjected to mean lift L_w and drag D_w at distance a ahead of the center of gravity and height h above it, and the tailplane is subjected to the mean lift L_t and drag D_t at a distance b behind the center of gravity. Static equilibrium of the forces follows

$$\begin{aligned} 0 = M_w + M_T = &-a(L_w\cos\alpha + D_w\sin\alpha) \\ &-h(L_w\sin\alpha - D_w\cos\alpha) + b(L_T\cos\alpha + D_T\sin\alpha) \end{aligned} \tag{11}$$

A counterclockwise perturbation of body pitch (above the level) by $-\Delta\theta_b$ raises the angle of attack $\Delta\alpha = \Delta\theta_b$ to both the wings and tail. Then, the rigid tail follows the body perturbation instantly, but the flexible wings lag behind because of their flexibility. As a result of the difference in response speed, the tail effectively presents a small stabilizing moment ΔM_T that tends to suppress the perturbation $-\Delta\theta_b$ following

$$\frac{\Delta M_T}{\Delta\theta_b} = -b\left(\frac{\Delta L_T}{\Delta\theta_b}\cos\alpha + \frac{\Delta D_T}{\Delta\theta_b}\sin\alpha\right) \tag{12}$$

This stabilizing tail moment at neutral elevation is small at slow glide speed, in comparison to that at maximum elevator. This free stream–induced moment is clearly not enough to stabilize powered forward flight, but the thrust-induced tail moment helps stabilize it. With passive stability in dual flight modes, this ornithopter shows potential to perform controlled flight.

The triple roles of wings for propulsion, lift, and drag are a notable advantage of flapping wing aircraft over rotorcraft, airplanes, paraglider, or hybrids thereof (*75*, *76*). Our work exploited these advantages of flapping wings and demonstrated aggressive flight maneuvers simply by tail control. These aggressive modes of flight include hover, high-speed dart, and an aerobatic turn while climbing.

A rapid aerobatic turn can be readily maneuvered by stopping an aerial dart or dive, initiated from high flight speed. Reversing the flight path could help the ornithopter avoid collisions in cluttered indoor spaces. Soaring theory and experiments show that a parachute effect can help an ornithopter soar to 90° just like gliding animals. A further flip upside down is made possible by tail elevation and wing dynamic stall at high translation speed in a soaring maneuver. This ornithopter recovered to glide stability without tumbling after a 90° body flip. We showed that the tail plays a dominant role in stabilizing powered flight and glide, whereas flexibility of wings lessened the destabilizing effect of its forward placement. In comparison, forward placement of canard surfaces (small forewings) of an airplane ahead of the main wing tends to destabilize flight if not properly trimmed (*30*, *31*).

Forceful propulsion is compulsory to power a hover and a dart before this aerobatic maneuver and to command flight control at various speeds. Here, we have developed an effective motorized drive for flapping wings with a low-loss transmission that incorporates an anti-whirl feature and elastic storage. We experimentally showed that flapping wing propulsion can be as forceful as propeller propulsion under the drive of the same motor, with the former being 40% more energetically efficient than the latter. Also proven was a linear relationship between frictional power loss and aerodynamic power and a linear relationship between output thrust and electrical power input. With this theoretical understanding, a better drive can be developed in the future to power ornithopters.

MATERIALS AND METHODS

Figure 1A and fig. S1 show our 26-g prototype of the tailed ornithopter with flexible X wings of 280-mm span. The X wings, which are configured in two crossing diagonal pairs, can clap and fling (open and close), each at a stroke angle of 50°. To command aerobatic maneuvers, this ornithopter is equipped with a relatively large tail. The fuselage of this ornithopter is 200 mm long. The body pitching inertia of this ornithopter is 284.8×10^{-6} kg m^2 as measured from pendulum oscillation. As shown in fig. S1, plumb line method found its center of mass behind the wing leading edges by 78 mm and ahead of the wing trailing edge by 5.4 mm. The tail leading edge is 98.5 mm behind the center of gravity.

Design and material selections were important to the realization of forceful and efficient propulsion. To improve the drive, we incorporated the following features to the double crank-rocker mechanism. First, a highly geared transmission helps maximize the load torque output and electromechanical conversion efficiency of the brushless electric motors. Second, a tandem pair of miniature ball bearings was introduced to each rotating shaft in the gear train. Third, a lightweight rigid housing made of carbon-reinforced polymer was used to hold the gear train. A tandem pair of nylon hinges for the wing bases was developed for partial elastic storage and as a guide to constrain the reciprocating crank/rocker. Anchoring the tandem wing pair to the fuselage also helped suppress the rocking motion induced by the wings. Nylon 6 was used to sustain the high crank force acting directly on the hinges, in replacement of previous polyimide film hinges (see fig. S6) (*47*, *49*). Apart from the careful design and construction of the drive, we also toughened the flexible wing construction by using tear-resistant polyurethane elastomeric membrane in addition to bat-like skeletal reinforcement by carbon spars.

Transmission: Fabrication and characterization

Figure 2D shows a transmission consisting of a rigid gearbox housing made from a carbon-fiber reinforced plate, shaft bearings, and a brass compound gear and two Delrin spur gears for intermediate and output coupling, respectively. This indirect drive could magnify the motor output torque by 76.8 times using a gear train with a 21.3 gear ratio and a crank-rocker mechanism with 3.6 crank ratio (i.e., 180°/50°). The brass compound spur gear had 32 outer teeth and 8 pinion teeth. Each of the Delrin spur gears had 48 teeth. Delrin was chosen for its self-lubricating properties. Rigid designs of

carbon-fiber plate housing and brass gears helped minimize load-induced deformation. When fixed to the rigid housing, bearing supports aligned the rotating shaft, thus reducing friction. Each of the shaft bearings (DDL301 miniaturized ball bearing as supplied by International Bearing Pte. Ltd, Singapore) weighed 0.04 g, with a 3-mm outer diameter, 1-mm inner bore diameter, and 1-mm thickness.

Figure S2 (A to C) shows the nylon flexure joints supporting the flapping wings, thereby helping recover the wing kinetic energy as elastic energy. As used for fishing line (*77*), nylon is well known for high toughness, high yield strain, and high ultimate elongation. Each nylon hinge was 0.5 mm thick, 1.5 mm long, and 3 mm wide; it can be bent elastically up to 68.8°. Two nylon flexures were staggered at a distance while pivoting the leading-edge spar of a wing pair. Two tandem nylon flexures arranged in this way avoided twist-induced fatigue caused by flapping loads. Our experiment showed that these nylon joint can sustain repeated bending (over 50° wing stroke) without failure during the course of a normal flying mission. In comparison, flexure joints of Delrin (a brand of acetal resin, polyoxymethylene) broke within a minute under the same conditions.

Elastic properties of the elastic hinge were measured by applying a load increment while measuring wing stroke with video or still images. Here, a six-axis force/torque sensor (ATI Nano 17) was used to measure the load torque. A digital camera was used to capture the wing stroke angle (equal to the hinge bending angle) under the applied load. Figure S2 shows two tandem nylon flexures having a linear torsional stiffness of 12.9 mN·m/rad. The no-load neutral position of the nylon flexures was measured to be 5°. The elastic energy (2*PE*) stored in the nylon hinges is calculated as the integral of the measured moment required to bend the hinge with respect to the angular wing stroke. Given a constant wing stroke amplitude of 50°, the calculated elastic energy storage was about 4.5 mJ, independent of wingbeat frequency. When the hinged wing pair was released from loading, its damped free oscillation measured a damped natural frequency of about 5 Hz.

As a benchmark, fig.S2A shows a rigid-body (double crank-rocker) mechanism with pin joints having little elastic energy storage. The mechanism is made of elastic linkages of acetal (polyoxymethylene) with self-lubrication, and pin joints, assembled in the same housing with shaft bearings. In addition, we included a radial stop (i.e., a protrusion as shown in fig. S2) at the root of the crank link to prevent the mechanism from being jammed to a dead toggling position. This radial stop does not brake the wing when it is not in contact at the mid-stroke where the wing stroke speed peaks. When the wing stroke exceeds 50°, the radial stop collides with the ground body frame. This pin-joint with the radial stop exhibited nonlinearly increasing stiffness for a stroke beyond 50° due to elastic deformation in the linkages and ground frame.

Wings and tails: Fabrication and characterization

Figure S2D shows the flexible wings consisting of elastic membrane (23-μm-thick polyurethane film, ArgoGuard 46510) and veined reinforcement by carbon rods that were adhesively taped onto the membrane like the bat digital skeletal structure in planform. The wing membrane had root chord fixed to the body, whereas its reciprocating leading edge was reinforced by a D-shaped carbon spar of 1-mm diameter. Chordwise veins attached to the membrane wings were made of 0.5-mm-diameter carbon rods, which were spaced at gaps from the leading-edge spar with membrane flexures. This chordwise wing flexibility allowed inertially induced passive wing rotation (*73*). Limiting the passive wing rotation was the membrane tension, root-chord support, and leading edge. There was some slack in the membrane wing. The mid-span chordwise rib could rotate under gravity for 11° about the leading edge. It could further rotate, for example, 24° under an extra 3-g load acting on the tip of the mid-span chord rib. Each of two diagonal pairs of flexible wings had a 280-mm span and 88-mm root chord width and weighed 1.82 g (with moment of inertia being 13.07×10^{-6} kg m^2). Each diagonal wing plane had a total plane area of 25.2×10^{-3} m^2.

Figure 1A shows a cross-tail control consisting of a static vertical stabilizer plane and a movable elevator plane. The horizontal tail has a total tail plane area of 8.9×10^{-3} m^2, whereas the movable part has an area of 5.6×10^{-3} m^2. This tail area is relatively large, about 35% of the wing plane area. The cross-tail planes were made of carbon-spar reinforced 1-mm-thick styrofoam (Depron). Servo motors weighing 1.7 g each were rated to a maximum torque of 7.36 mN·m at 4.2 V.

During static thrust testing, the ornithopter was mounted on a six-axis load cell as described above. A high-speed camera (Photron FASTCAM 1024 PCI) was used to study the wing kinematics. Video tracking of the leading-edge spar and the projected length of the mid-chord rib yielded the average wing stroke $2\phi(t)$ (off the horizontal reference where the wings close) and wing pitch amplitude $\beta(t)$.

SUPPLEMENTARY MATERIALS

robotics.sciencemag.org/cgi/content/full/5/44/eaba2386/DC1

Text

Fig. S1. Longitudinal dimensions and weight breakdowns of the X-winged tailed ornithopter.

Fig. S2. Elastic properties of hinges for flapping flexible wings.

Fig. S3. Transition between hovering and angled forward flight by elevator control under nearly constant throttle.

Fig. S4. Height dip when the ornithopter transited too fast from hover to forward flight, followed by a continuation of high-speed dart when the ornithopter was not pitched up in time.

Fig. S5. Time histories of flight distance, altitude and angles during stick-free nose-down glide as extracted from data in Fig. 8 and movies S7 and S8.

Fig. S6. Comparison between our previous design (240-mm span) and current design (280-mm span).

Fig. S7. Measurement setup for the propeller.

Fig. S8. Reported electrical power loading (*T*/*IV*) with respect to body mass and motor mass, respectively.

Fig. S9. Feasibility of other drones to perform flight arrest.

Table S1. Specifications of propeller designs under test.

Table S2. Effects of axle whirling in different propulsion devices.

Table S3. Hovering performance of various reported X-wing ornithopters.

Movie S1. Top view showing the low-loss drive of flapping X wings on nylon hinges.

Movie S2. Side view showing the low-loss drive of flapping X wings on nylon hinges.

Movie S3. Vertical takeoff and ascent (climb).

Movie S4. Aerobatics performed by an X-winged ornithopter with nylon hinges for elastic energy storage.

Movie S5. Recovery of glide stability after a flip upside down.

Movie S6. Height dip during the fast hover-to-forward transition and subsequent high-speed dart.

Movie S7. Unpowered dive with tail at neutral position.

Movie S8. Unpowered dive with tail pre-elevated.

Movie S9. Pulling up a dive and climb to hover.

REFERENCES AND NOTES

1. R. M. Alexander, *Principles of Animal Locomotion* (Princeton Univ. Press, 2003).
2. A. Biewener, *Animal Locomotion* (Oxford Univ. Press, 2003).
3. J. J. Videler, *Avian Flight* (Oxford Univ. Press, 2006).
4. W. Shyy, Y. Lian, J. Tang, D. Viieru, H. Liu, *Aerodynamics of Low Reynolds Number Flyers* (Cambridge Univ. Press, 2007).
5. P. Henningsson, L. C. Johansson, A. Hedenström, How swift are swifts *Apus apus*? *J. Avian Biol.* **41**, 94–98 (2010).
6. M. Marin, On the behavior of the black swift. *The Condor* **99**, 514 (1997).

7. Nat Geo WILD, Salivating for a new nest: Wild Borneo, 4 January 2017; http://youtube.com/watch?v=ngPs3kINUXE.
8. H. Y. Lim, J. K. I. Ho, *Aerodramus fuciphagus*—Edible-nest swiftlet, 02 January 2019; https://wiki.nus.edu.sg/display/TAX/Aerodramus+fuciphagus+-+Edible-nest+Swiftlet.
9. S. H. Ibrahim, W. C. Teo, A. Baharun, A study on suitable habitat for swiftlet farming. *J. Civil Eng. Sci. Technol.* **1**, 1–7 (2009).
10. D. Mackenzie, A flapping of wings. *Science* **335**, 1430–1433 (2012).
11. N. Chronister, Full history of ornithopters (2017); https://ornithopter.org/history.full.shtml [accessed March 2017].
12. A. Ramezani, S.-J. Chung, S. Hutchinson, A biomimetic robotic platform to study flight specializations of bats. *Sci. Robot.* **2**, eaal2505 (2017).
13. K. Karydis, V. Kumar, Energetics in robotic flight at small scales. *Interface Focus* **7**, 20160088 (2017).
14. D. Lentink, S. R. Jongerius, N. L. Bradshaw, *Flying Insects and Robots* (Springer, 2009), pp. 185–205.
15. F. van Breugel, W. Regan, H. Lipson, From insects to machines. *IEEE Robot. Autom. Mag.* **15**, 68–74 (2008).
16. M. Keennon, K. Klingebiel, H. Won, A. Andriukov, *AIAA Aerospace Sciences Meeting* (AIAA, 2012), pp. 1–24.
17. C. Richter, H. Lipson, Untethered hovering flapping flight of a 3D-printed mechanical insect. *Artif. Life* **17**, 73–86 (2011).
18. L. Ristroph, S. Childress, Stable hovering of a jellyfish-like flying machine. *J. R. Soc. Interface* **11**, 20130992 (2014).
19. Q. V. Nguyen, W. L. Chan, M. Debiasi, Experimental investigation of wing flexibility on force generation of a hovering flapping wing micro air vehicle with double wing clap-and-fling effects. *Int. J. Micro Air Veh.* **9**, 187–197 (2017).
20. Y. Nan, M. Karásek, M. E. Lalami, A. Preumont, Experimental optimization of wing shape for a hummingbird-like flapping wing micro air vehicle. *Bioinspir. Biomim.* **12**, 026010 (2017).
21. Q.-V. Nguyen, W. L. Chan, Development and flight performance of a biologically-inspired tailless flapping-wing micro air vehicle with wing stroke plane modulation. *Bioinspir. Biomim.* **14**, 016015 (2018).
22. J. DeLaurier, An ornithopter wing design. *Can. Aeronaut. Space J.* **40**, 10–18 (1994).
23. K. D. Jones, C. J. Bradshaw, J. Papadopoulos, M. F. Platzer, Bio-inspired design of flapping-wing micro air vehicles. *Aeronaut. J.* **109**, 385–393 (2005).
24. P. Zdunich, D. Bilyk, M. MacMaster, D. Loewen, J. DeLaurier, R. Kornbluh, T. Low, S. Stanford, D. Holeman, Development and testing of the mentor flapping-wing micro air vehicle. *J. Aircr.* **44**, 1701–1711 (2007).
25. Y. Kawamura, S. Souda, S. Nishimoto, C. P. Ellington, *Bio-Mechanisms of Swimming and Flying* (Springer, 2008), pp. 319–330.
26. G. C. H. E. De Croon, K. M. E. De Clercq, R. Ruijsink, B. Remes, C. De Wagter, Design, aerodynamics, and vision-based control of the DelFly. *Int. J. Micro Air Veh.* **1**, 71–97 (2009).
27. T. Nakata, H. Liu, Y. Tanaka, N. Nishihashi, X. Wang, A. Sato, Aerodynamics of a bio-inspired flexible flapping-wing micro air vehicle. *Bioinspir. Biomim.* **6**, 045002 (2011).
28. H.-K. Jung, J.-S. Choi, C. Wang, G.-J. Park, Analysis and fabrication of unconventional flapping wing air vehicles. *Int. J. Micro Air Veh.* **7**, 71–88 (2015).
29. K. D. Jones, M. F. Platzer, *Handbook of Unmanned Aerial Vehicles* (2015), pp. 1359–1383.
30. A. C. Kermode, *Mechanics of Flight* (Longman Scientific & Technical, 1987).
31. R. H. Barnard, D. R. Philpott, *Aircraft Flight: A Description of the Physical Principles of Aircraft Flight* (Pearson Education, 2010).
32. M. Karásek, F. T. Muijres, C. De Wagter, B. D. Remes, G. C. H. E. de Croon, A tailless aerial robotic flapper reveals that flies use torque coupling in rapid banked turns. *Science* **361**, 1089–1094 (2018).
33. N. T. Jafferis, E. F. Helbling, M. Karpelson, R. J. Wood, Untethered flight of an insect-sized flapping-wing microscale aerial vehicle. *Nature* **570**, 491–495 (2019).
34. X. Yang, Y. Chen, L. Chang, A. A. Calderón, N. O. Pérez-Arancibia, Bee$^+$: A 95-mg four-winged insect-scale flying robot driven by twinned unimorph actuators. *IEEE Robot. Autom. Lett.* **4**, 4270–4277 (2019).
35. Y. Chen, H. Zhao, J. Mao, P. Chirarattananon, E. F. Helbling, N.-S. P. Hyun, D. R. Clarke, R. J. Wood, Controlled flight of a microrobot powered by soft artificial muscles. *Nature* **575**, 324–329 (2019).
36. R. J. Wood, The first takeoff of a biologically inspired at-scale robotic insect. *IEEE Trans. Robot.* **24**, 341–347 (2008).
37. K. Y. Ma, P. Chirarattananon, S. B. Fuller, R. J. Wood, Controlled flight of a biologically inspired, insect-scale robot. *Science* **340**, 603–607 (2013).
38. M. H. Dickinson, F.-O. Lehmann, S. P. Sane, Wing rotation and the aerodynamic basis of insect flight. *Science* **284**, 1954–1960 (1999).
39. F. Leys, D. Reynaerts, D. Vandepitte, Outperforming hummingbirds' load-lifting capability with a lightweight hummingbird-like flapping-wing mechanism. *Biol. Open* **5**, 1052–1060 (2016).
40. T. Weis-Fogh, Quick estimates of flight fitness in hovering animals, including novel mechanisms for lift production. *J. Exp. Biol.* **59**, 169–230 (1973).
41. G. R. Spedding, T. Maxworthy, The generation of circulation and lift in a rigid two-dimensional fling. *J. Fluid Mech.* **165**, 247–272 (1986).
42. R. Madangopal, Z. A. Khan, S. K. Agrawal, Biologically inspired design of small flapping wing air vehicles using four-bar mechanisms and quasi-steady aerodynamics. *J. Mech. Des.* **127**, 809–816 (2005).
43. S. S. Baek, K. Y. Ma, R. S. Fearing, *2009 IEEE/RSJ International Conference on Intelligent Robots and Systems* (IEEE, 2009), pp. 2854–2860.
44. R. Sahai, K. C. Galloway, R. J. Wood, Elastic element integration for improved flapping-wing micro air vehicle performance. *IEEE Trans. Robot.* **29**, 32–41 (2013).
45. L. Hines, D. Campolo, M. Sitti, Liftoff of a motor-driven, flapping-wing microaerial vehicle capable of resonance. *IEEE Trans. Robot.* **30**, 220–232 (2014).
46. D. Campolo, M. Azhar, G.-K. Lau, M. Sitti, Can DC motors directly drive flapping wings at high frequency and large wing strokes? *IEEE/ASME Trans. Mech.* **19**, 109–120 (2014).
47. G.-K. Lau, Y.-W. Chin, J. T.-W. Goh, R. J. Wood, Dipteran-insect-inspired thoracic mechanism with nonlinear stiffness to save inertial power of flapping-wing flight. *IEEE Trans. Robot.* **30**, 1187–1197 (2014).
48. J. M. Kok, G. K. Lau, J. S. Chahl, On the aerodynamic efficiency of insect-inspired micro aircraft employing asymmetrical flapping. *J. Aircr.* **53**, 800–810 (2016).
49. Y.-W. Chin, Z. Ang, Y. Luo, W.-L. Chan, J. S. Chahl, G.-K. Lau, Spring-assisted motorized transmission for efficient hover by four flapping wings. *J. Mech. Robot.* **10**, 061014 (2018).
50. B. Bruggeman, "Improving flight performance of Delfly ii in hover by improving wing design and driving mechanism," thesis, TU Delft, Delft, The Netherlands (2010).
51. J. H. Marden, Maximum lift production during takeoff in flying animals. *J. Exp. Biol.* **130**, 235–258 (1987).
52. D. Floreano, R. J. Wood, Science, technology and the future of small autonomous drones. *Nature* **521**, 460–466 (2015).
53. N. Lomas, Is it a bird? Is it a bug? No it a biomimetic microdrone with flapping wings (2017); https://techcrunch.com/2017/03/25/is-it-a-bird-is-it-a-bug-no-its-a-biomimetic-microdrone-with-flapping [accessed 25 March 2017].
54. J. W. Kruyt, E. M. Quicazán-Rubio, G. F. van Heijst, D. L. Altshuler, D. Lentink, Hummingbird wing efficacy depends on aspect ratio and compares with helicopter rotors. *J. R. Soc. Interface* **11**, 20140585 (2014).
55. U. Pesavento, Z. J. Wang, Flapping wing flight can save aerodynamic power compared to steady flight. *Phys. Rev. Lett.* **103**, 118102 (2009).
56. S. Sunada, K. Tsuji, Advantages of an ornithopter versus an airplane with a propeller. *Trans. Jpn. Soc. Aeronaut. Space Sci.* **56**, 277–285 (2013).
57. E. W. Hawkes, D. Lentink, Fruit fly scale robots can hover longer with flapping wings than with spinning wings. *J. R. Soc. Interface* **13**, 20160730 (2016).
58. J. Grasmeyer, M. Keennon, *39th Aerospace Sciences Meeting and Exhibit* (2001), 127 p.
59. A. M. Harrington, C. Kroninger, Characterization of small DC brushed and brushless motors, Technical report, Army Research Lab Aberdeen Proving Ground MD Vehicle Technology Directorate (2013).
60. J. Winslow, M. Benedict, V. Hrishikeshavan, I. Chopra, Design, development, and flight testing of a high endurance micro quadrotor helicopter. *Int. J. Micro Air Veh.* **8**, 155–169 (2016).
61. M. Ramasamy, T. E. Lee, J. G. Leishman, Flowfield of a rotating-wing micro air vehicle. *J. Aircr.* **44**, 1236–1244 (2007).
62. R. R. Van Nimwegen, Critical speed problems encountered in the design of high-speed turbomachinery. *SAE Trans.* **73**, 524–536 (1965).
63. W. H. Reed III, Propeller-rotor whirl flutter: A state-of-the-art review. *J. Sound Vib.* **4**, 526–544 (1966).
64. J. P. Den Hartog, *CHAPTER VI Rotating Machinery: 51 Gyroscopic Effects* (Courier Corporation, 1985).
65. J. D. DeLaurier, An aerodynamic model for flapping-wing flight. *Aeronaut. J.* **97**, 125–130 (1993).
66. A. L. Thomas, G. K. Taylor, Animal flight dynamics I. Stability in gliding flight. *J. Theor. Biol.* **212**, 399–424 (2001).
67. G. K. Taylor, A. L. R. Thomas, Animal flight dynamics II. Longitudinal stability in flapping flight. *J. Theor. Biol.* **214**, 351–370 (2002).
68. Z. E. Teoh, S. B. Fuller, P. Chirarattananon, A hovering flapping-wing micro-robot with altitude control and passive upright stability, in *2012 IEEE/RSJ International Conference on Intelligent Robots and Systems* (IEEE, 2012), pp. 3209–3216.
69. J. A. Koopmans, S. Tijmons, C. De Wagter, G. de Croon, Passively stable flapping flight from hover to fast forward through shift in wing position. *Int. J. Micro Air Veh.* **7**, 407–418 (2015).
70. J. Moore, R. Cory, R. Tedrake, Robust post-stall perching with a simple fixed-wing glider using LQR-Trees. *Bioinspir. Biomim.* **9**, 025013 (2014).
71. M. T. Pope, C. W. Kimes, H. Jiang, E. W. Hawkes, M. A. Estrada, C. F. Kerst, W. R. T. Roderick, A. K. Han, D. L. Christensen, M. R. Cutkosky, A multimodal robot for perching and climbing on vertical outdoor surfaces. *IEEE Trans. Robot.* **33**, 38–48 (2016).

72. A. T. Conn, S. C. Burgess, C. S. Ling, Design of a parallel crank-rocker flapping mechanism for insect-inspired micro air vehicles. *Proc. Inst. Mech. Eng. Pt. C J. Mech. Eng. Sci.* **221**, 1211–1222 (2007).
73. A. R. Ennos, The inertial cause of wing rotation in diptera. *J. Exp. Biol.* **140**, 161–169 (1988).
74. J. D. Anderson Jr., *Introduction to Flight* (McGraw-Hill Higher Education, ed. 5, 2004).
75. D. Lentink, M. H. Dickinson, Biofluiddynamic scaling of flapping, spinning and translating fins and wings. *J. Exp. Biol.* **212**, 2691–2704 (2009).
76. J. Chahl, Unmanned Aerial Systems (UAS) Research Opportunities. *Aerospace* **2**, 189–202 (2015).
77. C. S. Haines, M. D. Lima, N. Li, G. M. Spinks, J. Foroughi, J. D. W. Madden, S. H. Kim, S. Fang, M. Jung de Andrade, F. Göktepe, Ö. Göktepe, S. M. Mirvakili, S. Naficy, X. Lepró, J. Oh, M. E. Kozlov, S. J. Kim, X. Xu, B. J. Swedlove, G. G. Wallace, R. H. Baughman, Artificial muscles from fishing line and sewing thread. *Science* **343**, 868–872 (2014).

Acknowledgments: We are grateful to B. D. Remes, M. Karásek, and G. C. H. E. (Guido) de Croon of Delft University of Technology for useful comments on the design of clapping X wings. **Funding:** Y.-W.C. acknowledges the Nanyang Technological University for providing a Nanyang Research Scholarship. J.M.K. acknowledges the Defence Science and Technology Group, Australia for supporting his fellowship in an exchange to Nanyang Technological University. The corresponding author G.-K.L. acknowledges the support by the Higher Education Sprout Project of the National Chiao Tung University and Ministry of Education (MOE), Taiwan. **Author contributions:** G.-K.L., Y.-W.C., J.S.C., and B.C.K. conceived the ideas and designed the study. Y.-W.C. designed and performed all experiments. Y.-W.C., Y.-Q.Z., and J.M.K. performed flight tests. Y.-W.C., J.M.K., Y.-Q.Z., and W.-L.C. implemented the electronic instrumentation. Y.-W.C. and G.-K.L. analyzed data. G.-K.L. derived theoretical models with the help of other co-authors. G.-K.L. and Y.-W.C. wrote the manuscript, whereas J.M.K. and J.S.C. wrote the section on aerobatics. All authors discussed the results and revised the manuscript. **Competing interests:** The authors declare that they have no competing interests. **Data and materials availability:** All data needed to evaluate the conclusions in the paper are present in the paper or the Supplementary Materials.

Submitted 16 November 2019
Accepted 18 June 2020
Published 22 July 2020
10.1126/scirobotics.aba2386

Citation: Y.-W. Chin, J. M. Kok, Y.-Q. Zhu, W.-L. Chan, J. S. Chahl, B. C. Khoo, G.-K. Lau, Efficient flapping wing drone arrests high-speed flight using post-stall soaring. *Sci. Robot.* **5**, eaba2386 (2020).

Science Robotics

Efficient flapping wing drone arrests high-speed flight using post-stall soaring

Yao-Wei Chin, Jia Ming Kok, Yong-Qiang Zhu, Woei-Leong Chan, Javaan S. Chahl, Boo Cheong Khoo, and Gih-Keong Lau

Sci. Robot. **5** (44), eaba2386. DOI: 10.1126/scirobotics.aba2386

Science Robotics (ISSN 2470-9476) is published by the American Association for the Advancement of Science. 1200 New York Avenue NW, Washington, DC 20005. The title *Science Robotics* is a registered trademark of AAAS.